

MEMS Gyroscope With Concentrated Springs Suspensions Demonstrating Single Digit Frequency Split and Temperature Robustness

Joan Giner^{ID}, *Member, IEEE*, Daisuke Maeda^{ID}, Kazuo Ono, Andrei M. Shkel^{ID}, *Fellow, IEEE*, and Tomonori Sekiguchi^{ID}, *Member, IEEE*

Abstract—We report on a new design approach for X-Y symmetric resonator, emphasizing the increase in symmetry by localization of the device anchors. The resonator is mechanized as a z-axis rate gyroscope (RG), and the concept is compatible with the rate-integrating gyroscope mechanization. Our approach is based on strategically placing the critical mechanical elements at the center of the resonator structure, to mitigate the effect of fabrication imperfections across the device. We experimentally demonstrated that the design yields a sub-Hz frequency separation between operational modes, which is attributed to the introduced design approach. The high symmetry of the device led to a temperature stability of 50 mHz over 130 °C temperature range. A ring down test demonstrated the Q -factor greater than 330 K. The thermal stability and preliminary characterization results of the gyro in-run stability are presented. [2017-0177]

Index Terms—MEMS gyroscope, frequency symmetry, Q -factor, thermal robustness.

I. INTRODUCTION

DYNAMICALLY balanced, degenerate-mode silicon MEMS gyroscopes [1], [2] are the candidates for precision rate and rate integrating operation. This technology can be utilized for GPS-challenged navigation, precision pointing platform stabilization of small systems and many other applications where small size, weight, power, high performance, and low cost are the requirements. Further improvement in the performance of MEMS Coriolis Vibratory Gyroscopes (CVG) will depend largely on the ability to achieve and maintain the frequency separation between the

drive and sense modes, preferably approaching $\Delta f = 0$, and to exhibit a high Q -factor for both operational modes. Two-dimensional resonators with low frequency split and high Q -factor have a potential to operate both as a rate gyroscope (RG) and a rate integrating gyroscope (RIG), in the former case removing the need for electronic integration of the rate output of the sensor producing the signal directly proportional to the rotational angle and increasing the detectable rate above the resonance frequency of the mechanical element. In addition, mechanical isotropy and frequency symmetry allow to operate the gyroscope interchangeably between the RG and RIG modes of operation, effectively increasing the full scale of operation while preserving its sensitivity when measuring low speeds of rotations.

A low frequency separation between the two principal axes of elasticity enhances the sensitivity of the sensor by reducing the thermomechanical noise and increasing the scale factor. When the device is operated in the RG mode, the reduction in frequency separation increases the sensitivity of the sensor. When the device is operated in the RIG mode, the low frequency separation allows to avoid “frequency locking” when measuring slow rotations, thus reducing the lowest threshold below which the sensor cannot detect any rotation, [3]. The symmetry requirements for avoiding the “locking” of the RIG mode device at low rotational rates are daunting. As an example, to measure in the RIG mode the Earth’s rotational rate, which is on the order of $\Omega = 15^\circ/\text{h}$, the frequency split of the device is required to be on the level of $\Delta f = 2 \cdot \Omega = 2 \cdot 15^\circ/\text{h} = 23 \mu\text{Hz}$. Such frequency symmetry is currently not practical for as-fabricated MEMS devices. This observation calls for the strategy to operate MEMS devices in the RG mode for low rotational rates and in the RIG mode for high rotational rates. The increase in the device symmetry is beneficial for both modes of operation, the RG and the RIG modes. The increase in the quality factor (Q -factor) is also beneficial for both modes of operation. In the RG mode, the sensor response amplifies proportionally to the Q -factor and in the RIG mode an increase in the Q -factor reduces the operational power and relaxes requirements on asymmetry of the device. Therefore, a higher symmetry and higher Q factor are equally desirable for a higher performance gyro, whether in the RG or RIG modes of operation.

Manuscript received August 9, 2017; revised July 23, 2018; accepted September 30, 2018. Date of publication November 28, 2018; date of current version February 1, 2019. Subject Editor A. Holmes. (*Corresponding author: Joan Giner.*)

J. Giner was with the Information Technology Department, Hitachi Research Laboratory, Hitachi 319-1221, Japan. He is now with the Technology Development-MEMS, GLOBALFOUNDRIES Pte. Ltd., Singapore 528830 (e-mail: joanginer@gmail.com).

D. Maeda is with the Sensor Design Department, Hitachi Automotive Systems, Ltd., Hitachinaka-shi 312-8503, Japan (e-mail: daisuke.maeda.bc@hitachi.com).

K. Ono and T. Sekiguchi are with the Information Technology Department, Hitachi Research Laboratory, Kokubunji 185-8601, Japan (e-mail: kazuo.ono.ap@hitachi.com).

A. M. Shkel is with the University of California at Irvine, Irvine, CA 92697 USA (e-mail: ashkel@uci.edu).

Color versions of one or more of the figures in this paper are available online at <http://ieeexplore.ieee.org>.

Digital Object Identifier 10.1109/JMEMS.2018.2881209

Conceptually, degenerate mode gyroscopes are designed to have the same drive and sense frequencies ($\Delta f = 0$). However, in practice, the fabrication process contributes to imperfections such as due to lithography and etching, among others, introducing imperfections in mass distribution and stiffness. Suspension springs are the most critical elements of the design since even minor changes in width or slope of etching strongly affects the resonance frequency of the two operational modes thus increasing the frequency separation. With the current state-of-the-art micro fabrication techniques, it seems not possible to manufacture silicon MEMS consistently with the level of frequency symmetry in the range of μHz . Therefore, highly precise postfabrication frequency tuning mechanisms have to be put in place to operate the gyroscope in the degenerate mode.

The Q -factor is a figure of merit that quantifies the capability of the MEMS resonator to preserve the mechanical energy of the system. There are several factors that may affect the Q -factor of the device: air damping, anchor losses, thermos-elastic damping (TED), and surface losses, to name a few dominant. Air damping is caused by interaction of the moving mass with the surrounding air particles, especially when the air is in between the moving structure and the fixed plates. Air damping is significantly reduced, even eliminated, when MEMS are operated in vacuum. In the case of anchor losses, the Q -factor is degraded when the mechanical energy flows from the mechanical structure to the substrate via anchors. Reduction of the anchor losses can be achieved by strategically placing the anchor in the mechanical nodes, achieving dynamically balanced structures or by reducing the number of anchors [4], [5]. In all cases, the design of the device is implemented to cancel the mechanical acoustic waves traveling to the substrate. Losses due to the thermos-elastic damping can be modeled and the MEMS can be optimized to minimize those losses. Both features, high Q -factor and low Δf , are the desirable features of the design to achieve high sensitivity and low drift.

To overcome the current fabrication limitation and achieve dynamically balanced symmetric MEMS resonators, the research community explored a number of alternatives that can be classified as either design-centered or fabrication-centered approaches. In the design-centered approaches, more conventional MEMS fabrication techniques are used and a mass-on-spring system is utilized to implement dynamically balanced resonators [6]–[10]. The use of inherently symmetric structures, such as rings and disks, were explored in [11]–[13]. In the fabrication-centered approaches some advanced fabrication techniques were also explored [14]–[17], aspired to replicate structural advantages on the micro-scale of the HRG-type device, [18] while also pursuing the structural symmetry and the quality factor.

Our review of literature suggests that in practice, with the current state-of-the-art silicon etching technology, it is not possible to obtain a highly symmetric as-fabricated modematched gyroscope, therefore post-fabricated frequency matching techniques will be required in the foreseen future to achieve the true modematched mechanical elements (at least in the order of 10-20 μm). In general, matching frequencies is

a two-stage process. First a rough tuning is performed after the fabrication in order to bring resonant frequencies as close to each other as possible, while preserving the dynamic balance. Then, a fine tuning is employed to reduce the frequency split to quasi-zero Hz and keep it stable through the temperature range of operation. Frequency tuning techniques can be implemented, either based on mechanical (permanent) and electrical/electronic (adaptive) adjustments. The mechanical approach is used as a rough tuning method and the electrostatic approach is used as a finetuning method. In most cases, the rough mechanical tuning is performed prior to the fine electrostatic tuning. Mechanical perturbations are introduced based on mass removal, [19], or mass addition, [20], to permanently change the mechanical frequencies. A more flexible alternative is based on electrostatic tuning of the operational modes with large as-fabricated frequency splits, [21], or small separation [22]. Electrostatic tuning presents several limitations. For a large tuning range, large electrostatic forces are required. This approach implies the use of a large area of electrodes or the use of large tuning DC voltages. It was reported that an increase in the tuning voltage has a negative effect on other structural parameters, such as the Q -factor, [7], and noise amplification. Thus, achieving the structural symmetry by increasing the tuning voltages is not a desirable option.

Resonant MEMS devices are fabricated using micro fabrication techniques at a wafer level. The resonant frequencies of mechanical elements vary across the wafer due to non-uniformity of fabrication steps, [23]. Non-uniformity of the fabrication process can be extrapolated to device-level or chip-level. Our design concept, for the first time introduced in [24], explored the idea of concentrating the critical parts of the design – the suspension elements – in a small central area of the device. This design strategy allowed us to mitigate a nonuniformity of etching across a single device and led to highly isotropic gyro structures, while keeping a high Q -factor due to XY symmetric “tuning-fork” dynamics. Our approach allowed to reduce electrostatic forces required to fine-tune the operational frequencies to achieve a better control of the frequency split and to reduce electrostatic forces applied to the mechanical structure. We utilized for this study the architecture introduced in [24].

This paper is structured as follows. In section II, we analyzed the effects of design on the frequency split and the Q -factor, and reported our simulation results of the proposed resonator. In section II, we also correlated the location of mechanical springs and anchors to the fabrication imperfection linking it to the frequency split. The fabrication process is reviewed in section III, followed by characterization results in section IV. We conclude the paper with section V, providing conclusions and outlook.

II. DESIGN FOR LOW FREQUENCY SPLIT AND HIGH Q -FACTOR

A. Effects of Δf and Q -Factor on Gyro Performance

Frequency mismatch and Q -factor influence the sensitivity and drift of Rate Gyroscope (RG) and Rate Integrating Gyroscope (RIG). In the mode matched operation, the scale

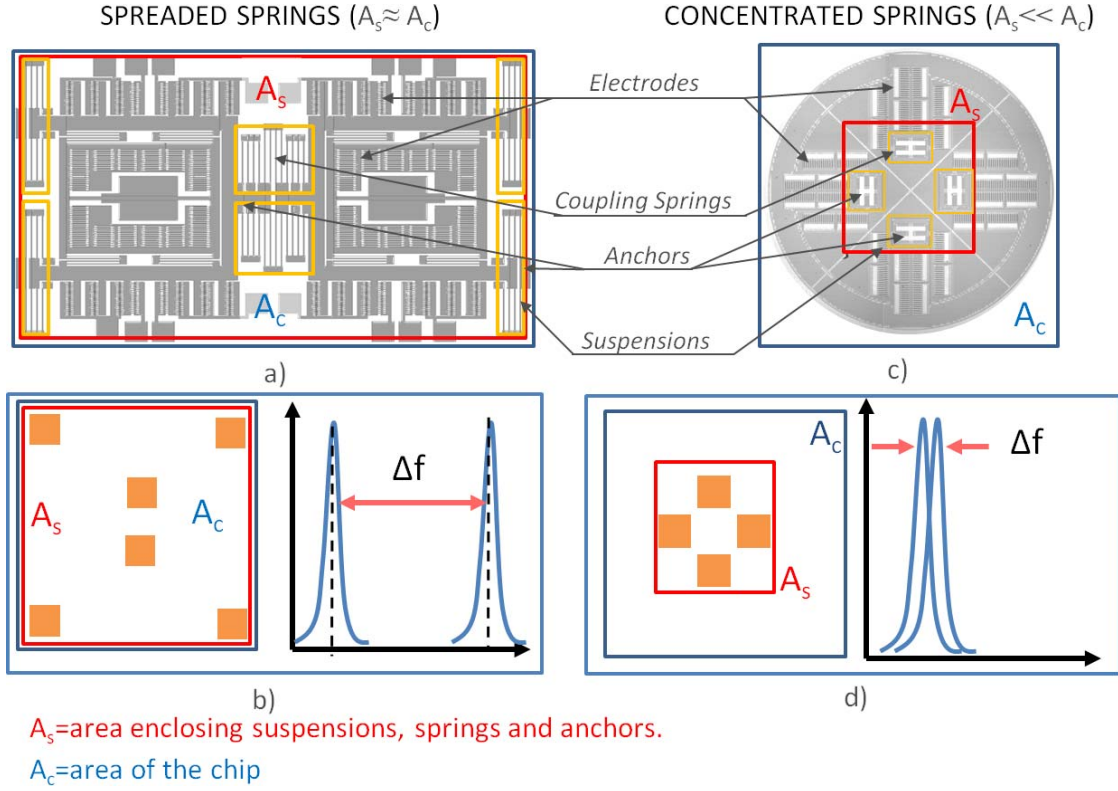


Fig. 1. Illustration of the concept of concentrated springs. In a), shown is the tuning fork presented in [25], with springs distributed along the perimeter and at the center of the chip area. In b), a simplified diagram is shown illustrating the area of the spring A_s and the area of the chip A_c of the design in a); In c), a conceptual layout of the devices is presented, which is the focus of this work, emphasizing the importance of springs location close to the center of the chip; In d), the corresponding A_s and A_c of the design in c).

factor of the RG is amplified by the Q -factor, providing higher rate sensitivities and lower Mechanical-Thermal Noise (MTN). The effects of the frequency mismatch and the Q -factor on the MTN are discussed in [25]. MTN is a noise mechanism caused by the Brownian motion of the sense-mode appearing in the gyro output as angle random walk (ARW). In the RIG mode of operation, the resolution of the angle measurements depends on frequency asymmetry of the device in damping and frequency, which arises from fabrication imperfections. The Q -factor, damping asymmetry, and frequency split are setting the limit on the gyro minimum detectable angle in the RIG mode of operation. The gyroscope drift due to non-idealities can be estimated as

$$\Omega_{error} = \Delta \left(\frac{1}{\tau} \right) + \frac{1}{\tau} \frac{\Delta f}{f}, \quad (1)$$

where $\Delta(1/\tau)$ is the difference between inverse of the decay time, $1/\tau_1 - 1/\tau_2$, where τ_1 and τ_2 are the lowest and highest decay time of the resonator (corresponding to the principal axes of damping), $\Delta f = f_1^2 - f_2^2/f$, where f_1 and f_2 are the resonant frequencies of the X and Y modes, where X and Y are the principal axes of elasticity, and $\tau = Q/\pi f$ is the decay time for the corresponding Q -factor (quality factor) of the resonator.

B. Concentrated Springs Architecture

We illustrate the idea of concentrated springs architecture in Fig. 1. Fig. 1a shows a tuning fork gyroscope presented

in [26], as a representative example of the spread springs architecture. The dual-mass resonator is attached to the substrate via springs located in four corners (and also at the center). Mechanical coupling springs are located at the center of the chip. In this architecture, the area of the springs A_s (enclosed by a red square in Fig. 1a) is the same as the area of the chip A_c (enclosed in a blue square in Fig. 1b). The ratio of the spring area over the device area is A_s/A_c . Fig. 1b shows a schematics of the concept and a qualitative representation of the frequency split. In the concentrated springs architecture (Fig. 1c), mechanical suspensions and coupling springs are located close to the center of the chip, within a small area A_s , as compared to the area of the chip A_c . The concentrated spring architecture presents a ratio A_s/A_c smaller than 1.

For this work, we broadly surveyed the literature on mass-spring based MEMS gyroscopes, and compared the ratios between the area of springs and the area occupied by the corresponding device, A_s/A_c , and related that ratio to the as-fabricated frequency split reported in publications. Our approach is based on the observation and measurement of optical images provided by authors in the corresponding publications. In Fig. 2, we mapped devices with respect to their ratio A_s/A_c (a vertical axis), as a function of the as-fabricated frequency separation (a horizontal axis). Note that in this survey we excluded publications that did not use DRIE for the definition of structures, such as, for example, micro-hemispherical shells [14]–[17]. The literature survey

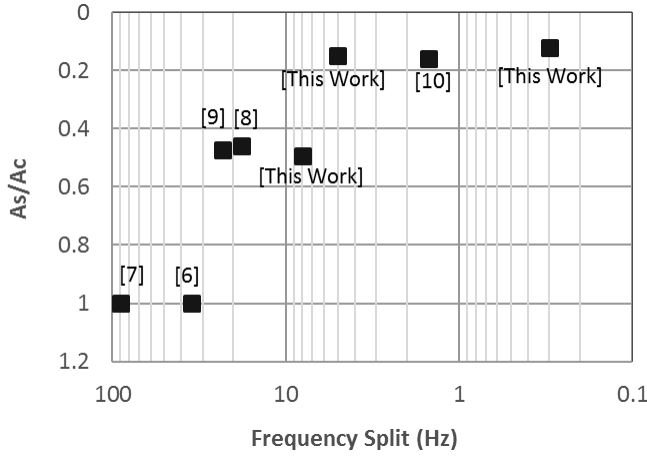


Fig. 2. Literature survey mapping approaches based on concentration of structural anchors relative to the design concept explored by this work. A_s and A_c are defined in Figure 1. Data suggests that devices with $A_s/A_c \approx 1$ are more susceptible to fabrication imperfections than devices with $A_s/A_c < 1$.

summarized in Fig.2 suggests a relationship between the ratio A_s/A_c and the as fabricated frequency split. We can observe that smaller as-fabricated frequency split can be obtained if the mass-spring gyroscope is designed with the springs located towards the center of the chip.

To further investigate the trend observed from the literature survey, we designed and fabricated test devices of two types, with ratios of A_s/A_c of 0.15 and 0.5, respectively, while keeping all other parameters the same. We mapped the explored design space of this paper in Fig. 2.

C. Concentrated Spring Design

Figure 3 shows a schematic representation of the resonator in operation. The design reported in this paper is based on two mechanically coupled concentric circular masses that share the same center of mass. Both proofmasses are designed to have the same mass and the same resonant frequencies. Masses are attached to the substrate by 4 anchors. The anchors are located between the two masses and mechanically connected to the masses via a pair of shuttles. The shuttles are connected to the inner and outer masses by suspension springs and are constrained to move with one degree of freedom, while allowing at the same time the inner and the outer masses to move freely in any direction in the XY plane.

Mechanical resonant frequencies of the two inner and outer masses have been designed to be the same. Fig 4 shows a schematic representation of the springs, anchors, and shuttles. Inner and outer masses are mechanically connected to the inner and outer shuttles, m_{s1} and m_{s2} , via springs with a spring constant k_m . Shuttles are connected to the anchor via springs with the spring constant k_a . The geometry of springs k_m and k_a is illustrated in Fig 4. The orientation of springs is chosen to be compliant in one direction and very stiff in a perpendicular direction. The spring constants of the U-shaped beams can be approximated by $EtW^3/2L^3$, where E , t , L and W are the Young's modulus, thickness, length, and width of each beam, respectively. The corresponding in-phase resonant frequencies

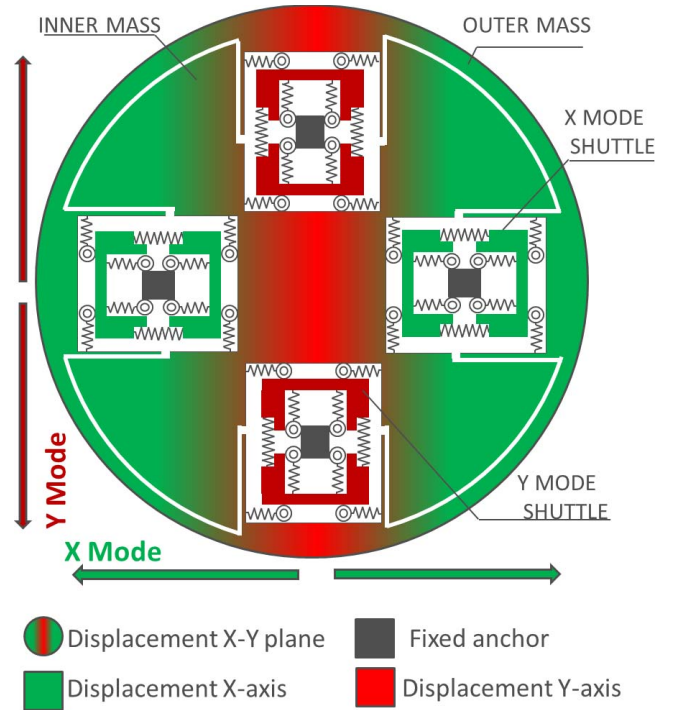


Fig. 3. Schematic representation of the investigated concentrated spring gyro architecture. Inner and outer masses are free to move along the X and Y axes (2 degrees of freedom) as indicated with green and red colors. Shuttles of the X axis move along the X direction (green) and shuttles of the Y axes move along the Y direction (red). This is a conceptual drawing, the geometry of suspensions and masses are not to scale. Structural elements with one degree of freedom are in solid colors, while elements with two degrees of freedom are in transitional colors.

ω_{ix} and ω_{iy} , are calculated as:

$$\omega_{ix} = \omega_{iy} = \sqrt{\frac{4(k_a + k_m)}{m_o + 2m_{s2}}} = \sqrt{\frac{4(k_a + k_m)}{m_i + 2m_{s1}}} \quad (2)$$

In this equation, k_a is the stiffness of the spring connecting the shuttle to the anchor, and k_m is the stiffness of the spring that joins the shuttles with the masses, and m_o , m_i , m_{s1} , m_{s2} are the masses forming an outer mass, an inner mass, an inner shuttle and an outer shuttle, respectively. The resonant frequency was set the same for the inner and outer masses along the X- and Y-axis. It is important to note that only two pairs of shuttles are accounted for the total effective mass, hence the factor of 2 in equation (2). The out-of-phase resonant frequency can be calculated using:

$$\omega_{ox} = \omega_{oy} = \sqrt{\frac{4(k_a + k_m) + 8k_c}{m_i + 2m_{s1}}} = \sqrt{\frac{4(k_a + k_m) + 8k_c}{m_o + 2m_{s2}}} \quad (3)$$

In this equation, k_c is the stiffness constant of the coupling beam with the geometry shown in Fig. 4. Design of the coupling spring was chosen to separate resonances of the in-phase and the out-of-phase mode by as much as 20%.

In the gyroscope operation, the resonator is excited in its outofphase mode. The resonant frequency of the out-of-phase mode depends largely on the mechanical properties of the coupling beam and can be estimated using equation (3).

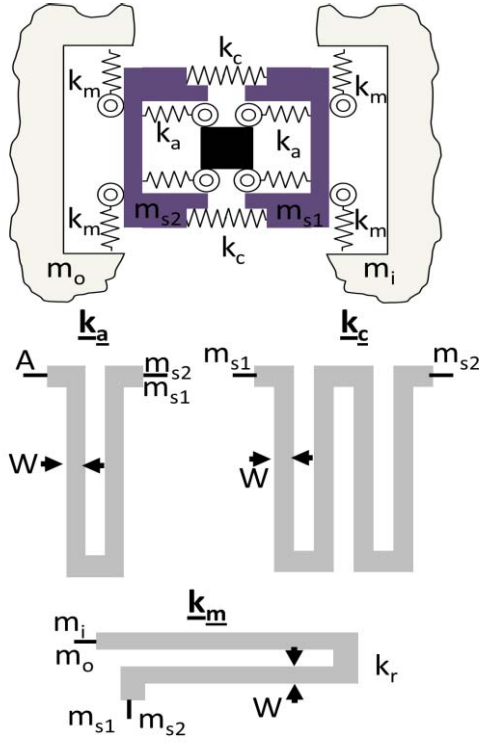


Fig. 4. Sketch of the spring-shuttle-anchor module. Orientation of the springs k_a , k , and k_c corresponds to the orientation of maximum compliance. Actual architecture of the springs is also included, as well as the connected masses.

TABLE I
WIDTH OF SUSPENSION OF FABRICATED SUSPENSION SPRINGS

Device	C006	C221	C298	S016	S281	S223
S1	6.48	5.6	6.38	6.42	6.15	5.56
S2	6.48	5.65	6.53	6.74	6.22	5.62
S3	6.42	5.55	6.34	6.48	5.96	5.55
S4	6.55	5.55	6.43	6.55	6.10	5.42
W_n	6.48	5.58	6.42	6.54	6.10	5.54
W_{var}	0.13	0.10	0.19	0.32	0.26	0.18

In this work, three different types of resonators were designed and implemented in order to study the effects of fabrication imperfections on different geometry of springs. In particular, the width of springs was designed to be 3, 5, and $10\mu\text{m}$ to achieve the resonant frequencies of the out-of-phase mode of 1.1, 3, and 10kHz, respectively. The mechanical parameters are listed in Table 1. Release holes were patterned on the silicon masses to provide a uniform access of the etchant to the sacrificial oxide layer for release of the structure (fabrication details are discussed in section III). The size and separation of the release holes were obtained by modeling the resonator using MEMS+ software package, [27] with the objective of maintaining the same mass for the inner and outer proofmasses. All three prototypes have been simulated using Coventorware [28] to obtain the theoretical thermos-elastic damping (TED). The solid models were meshed with more than 25000 elements to assure the convergence of Finite Element Analysis (FEA) calculations. The Q-factor limit due

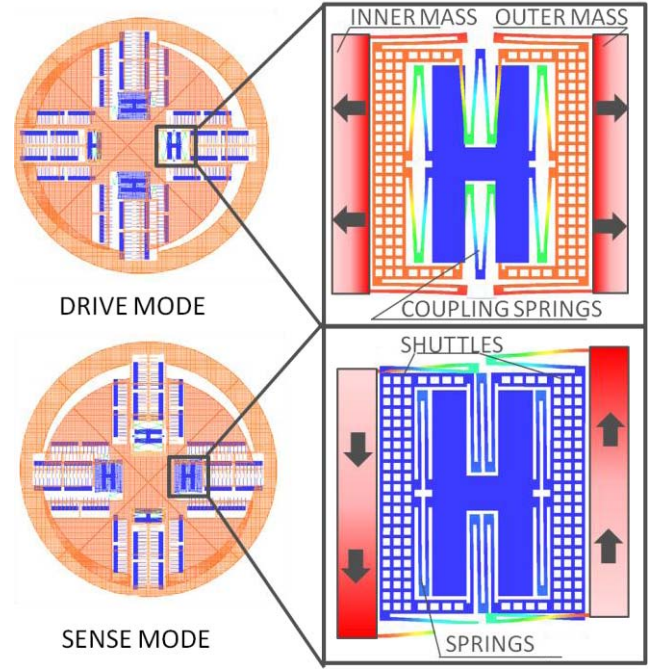


Fig. 5. FEA simulation of the tuning fork-like oscillations in an anti-phase degenerate mode. Shown are details of the shuttle and springs kinematics along the X and Y displacements of masses.

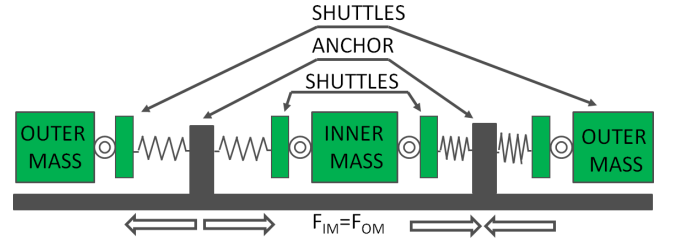


Fig. 6. Mass-balanced design includes the same inner and outer mass resulting in the same resonant frequency. The anti-phase oscillation cancels the mechanical forces at the anchors, mitigating the energy loss from device to substrate through the anchors.

to the TED was modeled to be 1.7M, 2.53M, 0.2M for the 1.2, 3, and 10kHz devices, respectively.

When in operation, the masses are forced to oscillate in an out-of-phase mode along the X or Y directions (a tuning-fork-like motion) by using electrostatic electrodes embedded inside the suspended masses. For the inner and outer masses, the same frequency of operation is achieved by implementing the coupling springs between the inner and the outer shuttles. During the operation, the two pairs of shuttles move in an outofphase motion with respect to the anchor and along the respective mass, while the equivalent and perpendicularly oriented pairs remain motionless, Fig 5. Unlike in a conventional tuning-fork the center of masses of the presented design remains centered during the operation canceling the reaction torques and forces in the area of anchors thus mitigating the mechanical energy leakage through the anchors, Fig 6.

Electrostatic actuation and capacitive sensing are achieved by 32 electrodes embedded in the masses, 16 for the inner mass and 16 for the outer mass. Each set of electrodes is

formed by 15 parallel plate capacitors. To allow a large displacement of the masses the gap between parallel plates is chosen to be $8\mu\text{m}$. The total drive or sense capacitance for each mass along either x or y-axis is 10pF .

In our approach the key element of the design is a compact architecture of the spring-shuttle-anchor module. In the presented design implementation the area of the suspension spring A_s is $2 \times 2\text{mm}$, and the area of sensing element A_c is $5.7 \times 5.7\text{mm}$, providing the ratio of $A_c/A_s = 0.12$. According to our survey of literature, Fig 3, this is the lowest ratio reported in the literature, and is believed to be a critical design parameter for achieving isotropy of the device. In the next section we will present our experimental results supporting the hypothesis on the influence of anchor concentration on structural symmetry of devices.

III. FABRICATION

An array of devices was fabricated using a single mask standard 6" SOI (100) process with a $60\mu\text{m}$ device layer thickness and $2\mu\text{m}$ buried oxide thickness. A stepper was used to define three different patterns of suspension springs on a $2.5\mu\text{m}$ photoresist coating, that was used as a mask for Deep Reactive Ion Etching (DRIE). The effective mass of the two concentric masses was kept the same for the three prototypes with only a significant variation introduced by widths of the springs, designed to be 3, 5 and $10\mu\text{m}$ resulting in 1.2, 3 and 10kHz resonance frequencies, respectively.

DRIE was performed for 35 minutes using a three-step standard Bosch process consisting of two cycles: breakthrough and etching. The breakthrough cycle etched the passivation layer at the bottom of the trench and cleared the way for the following etching sequence to etch the silicon isotropically. In both steps, the breakthrough and the etching, the coil was powered at 1500W , pressure inside the chamber was set to 3Pa , the flow of SF_6 was set to 400sccm and the platen bias was set to low frequency in order to mitigate the notch formation between the silicon and the dielectric. For the breakthrough, the etching time was 1.2 seconds and the platen power was 90W . The following etching step had the duration of 0.4s and the platen power of 20W . The deposition cycle had the duration of 1s , with the S_4F_8 flow at 400sccm , and the pressure set at 6Pa . The coil was powered at 1500W . The power was chosen to prevent overheating of the thin features such as the comb drive fingers and springs.

Figure 7 shows an optical image of the released device. A vapor HF-based release process was performed at a die level. The pressure inside the etcher was kept at 12Pa HF and N_2 flow was set to 250sccm and 50sccm , respectively.

IV. CHARACTERIZATION

A. Spring Location and Fabrication Imperfection

In section II.B we hypothesized, based on literature survey and findings in [23], that the use of concentrated spring architecture has a potential to reduce the effects of the fabrication tolerances on the frequency symmetry. In addition to devices described in Section III, we developed two additional designs to investigate the effect. We focused on the fabrication error

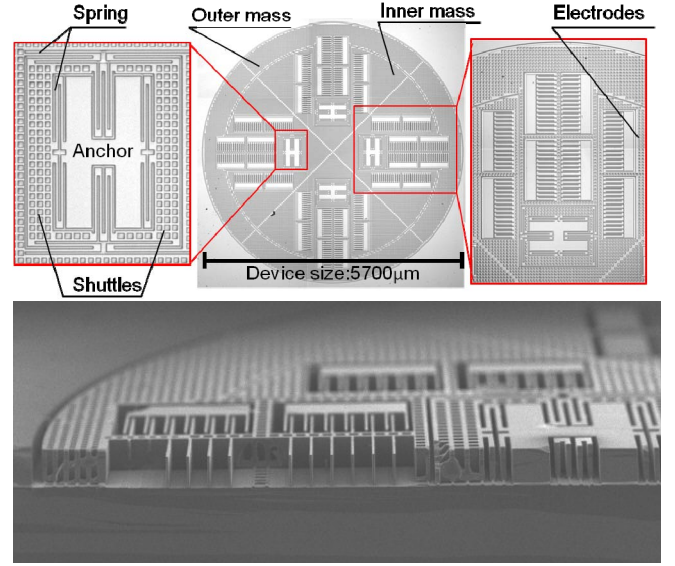


Fig. 7. Optical images of the gyroscope and a close up of electrodes and a spring-shuttle-anchor module.

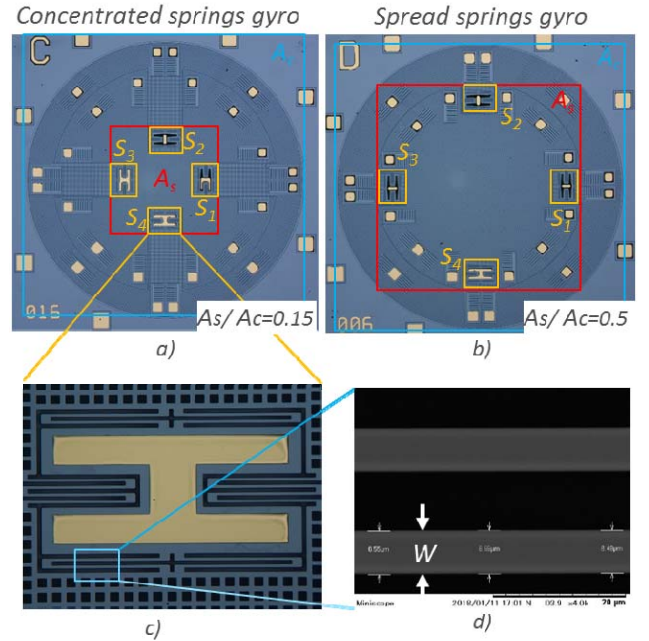


Fig. 8. (a) and (b) are the optical images of fabricated prototypes with concentrated ($A_s/A_s = 0.15$) and spread ($A_s/A_s = 0.5$) architectures. Anchors and springs are enclosed in the areas S_1 - S_4 . (c) shows the SEM image of the anchor and spring module taken with the Hitachi Miniscope TM3030. (d) The U-shaped spring width that connects the anchor with the outer shuttle is manually measured for each area S . Table I shows a larger variation of the width in the spread springs architecture.

introduced by the fabrication process before the resonator release step (e.g., exposure, patterning, and DRIE etching). The two test devices are shown in Fig.8. Optical image in Fig. 8(a) and (b) corresponds to the concentrated springs and the spread springs architectures, respectively. The resonator architecture was discussed in Section II.C. Both resonators are designed to have the same inner and outer masses as well as the spring width of $5\mu\text{m}$. The mass of the shuttles is also

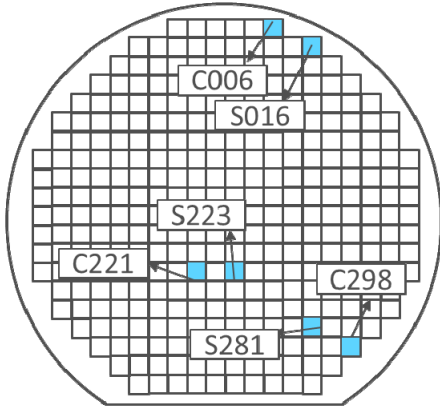


Fig. 9. Wafer map illustrating the position of the selected test resonator for measurements of the spring width variations.

the same in both cases. Simulations confirmed some close operational frequencies for both designs. The foot-print of both devices is enclosed inside the same area A_c in Fig.8 (a). The area of mechanical springs is enclosed inside the area A_s and is chosen intentionally different for the two designs. The position of each spring module is labelled from S_1 to S_4 . The ratio between the area of the springs and the area of the operational device were designed to be $A_c/A_s = 0.15$ and 0.5 for the concentrated and the spread architectures, respectively.

After devices were fabricated, we optically characterized 6 samples, with 3 concentrated spring and 3 spread spring designs. Fig. 9 shows the wafer map with highlighted position of the measured test devices. The meaning of the letters in front of the device number are explained as follows: the “S” subscript stands for “spreaded” while “C” stands for “concentrated”. We used Hitachi Miniscope TM 3030 SEM with a resolution of 10nm to measure manually the width of a U-shaped spring that mechanically connects the anchor with the outer shuttle, Fig.8 (c), for the four anchors (S_1 - S_4) of each device. To reduce the error introduced by the manual measurement, each beam was measured at 3-5 different locations and the readings were averaged to obtain the best estimation. Table 1 summarizes the results. The measured widths were also averaged to obtain an estimate of the nominal width of the beam (W_n) for each resonator. Variation of the width in each of the device was also calculated (W_{var}). Note that the nominal width of the U-shaped spring differed from device to device according to their position on the wafer, as suggested in [23]. Experimental results showed a larger variation of the width intra-device for those devices with spread architecture and lower variation for devices compared to those devices with concentrated springs located in a similar position on the wafer.

The width of the beams has a direct correlation with the resonator frequency of the operational modes, as indicated in equations (2) and (3). CoventorMP MEMS+ was used to investigate the effect of the width variation of the inner-device on the frequency separation. We developed a model for each of the two architectures and performed modal simulation introducing the measured widths. The nominal width across each device was set to the corresponding W_n , for each resonator. The width for each measured U-shaped

TABLE II
SIMULATION OF THE FABRICATION IMPERFECTIONS OF FREQUENCY SPLIT

Device	Ideal		w/ fabrication tolerances	
	Frequency (Hz)	Δf (Hz)	Frequency (Hz)	Δf (Hz)
C006	8639	0	8636	5
C221	6884.2	0	6884.3	1.5
C298	8476.8	0	8472.4	8.5
S016	8709	0	8691	26.2
S281	7825	0	7821.5	8.1
S223	6766	0	6766.1	32

C=Concentrated; S=Spread

TABLE III
FREQUENCY SPLIT CHARACTERIZATION

Device		Parameters	
		Nominal Frequency (Hz)	Δf (Hz)
$W_s=10\mu m$	#1	10363	3.1
	#5	10236.3	2.5
$W_s=5\mu m$	#7	3248.1	5.1
	#6	3159.2	7
	#2	3011	0.2
$W_s=3\mu m$	#4	1255	10
	#3	1172.4	0.3

spring in Fig.8(c) was accounted in the model. The modal simulation results are shown in Table 2. The second column shows the resonator frequency of the out-of-phase mode when no variation of the width is introduced in the model (ideal conditions) and considering a uniform nominal width of W_n for each resonator. The third column shows the corresponding frequency split. The fourth column shows the operational frequency of the out-of-phase mode in the x direction when imperfections are considered, and the fifth column shows the calculated frequency separation between the two operational modes. Simulation results showed a single digit frequency separation for the concentrated spring devices and a few tens of Hz for resonators with spread springs. It should be noticed that we limited our considerations to variations in 4 of the beams and assumed the rest of the beams to preserve the nominal width. We assumed that variations of the width will be similar for all the beams and therefore the simulation will remain consistent across the wafer.

B. Resonator Characterization

Released devices, designed using the approach introduced in section 2.C, were attached to ceramic packages using conductive epoxy and placed inside a custom built vacuum chamber. Figure 8 shows schematics of the characterization set-up. All DC voltages and the signal sources are generated using an FPGA-based lock-in amplifier Zurich Instruments, HF2LI [29]. Forcer electrodes, composed of 2 electrodes on one side of the inner mass and two opposite electrodes on the outer mass, for both drive and sense axes (yellow and black electrodes in Fig. 9), were connected to a signal generator with a 100mV amplitude. Inner and outer masses were driven in the out-of-phase mode. Drive and sense pick-off electrodes were connected to two trans-impedance amplifiers

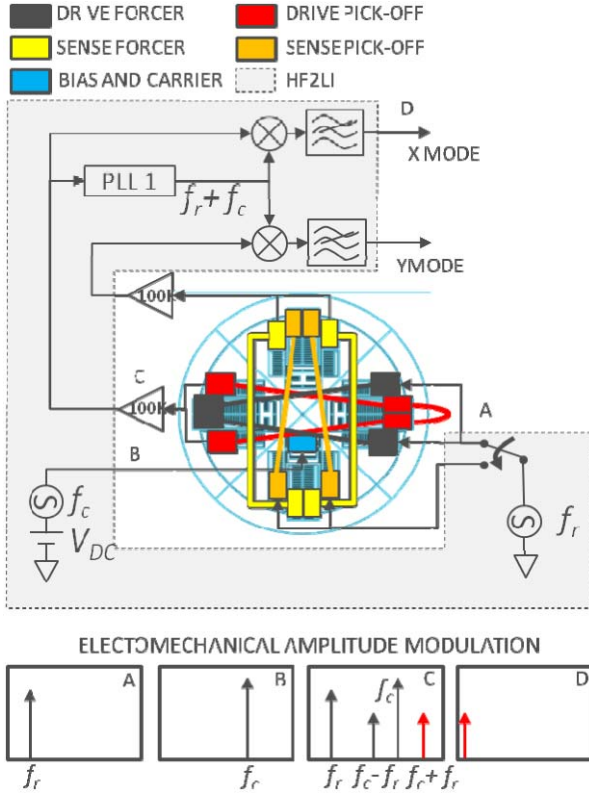


Fig. 10. Characterization set up for the resonator frequency response and the Q-factor measurement. The grey-shaded part corresponds to the element inside the FPGA-based Lock-in amplifier. The bottom part shows the frequency components at each point of the characterization setup.

HF2TA from Zurich Instruments. The suspended mass was connected to a DC voltage $V_{DC} = 6V$ and a carrier frequency generator of 100kHz. Out-of-phase mode was excited using a single-ended signal. Electromechanical Amplitude Modulation (EAM) technique was used to mitigate the effects of the parasitic capacitances introduced by the characterization set-up, such as vacuum chamber through connections and sockets. The EAM technique is outlined at the bottom part of Fig. 10. The input frequency, f_r (A), was used to excite the mechanical resonance of the MEMS, and the carrier signal, f_c (B), was applied to the proof-mass. Both signals were modulated by the micromechanical resonator. The modulated signal at the output of the resonator (C) has four main frequency components. The sideband frequencies components $f_c + f_r$ and $f_c - f_r$ contain the mechanical amplitude information. Therefore, a demodulation of the output signal at $f_c + f_r$ and a low-pass filtering allows to recover the pure mechanical amplitude.

To characterize the frequency response of the resonator, devices were placed in a vacuum chamber at moderate pressure of around 10Pa and the excitation frequency was swept around the resonant frequency f_r . The output was demodulated following the same scheme explained in the previous paragraph. This technique was applied for both x and y directions. The results for three types of resonators are shown in the left column of Fig. 11. The resonator at the 1.2kHz resonant frequency shows a frequency separation of 0.3Hz, the 3kHz device shows less than 0.2Hz separation whereas the 10.2kHz device shows

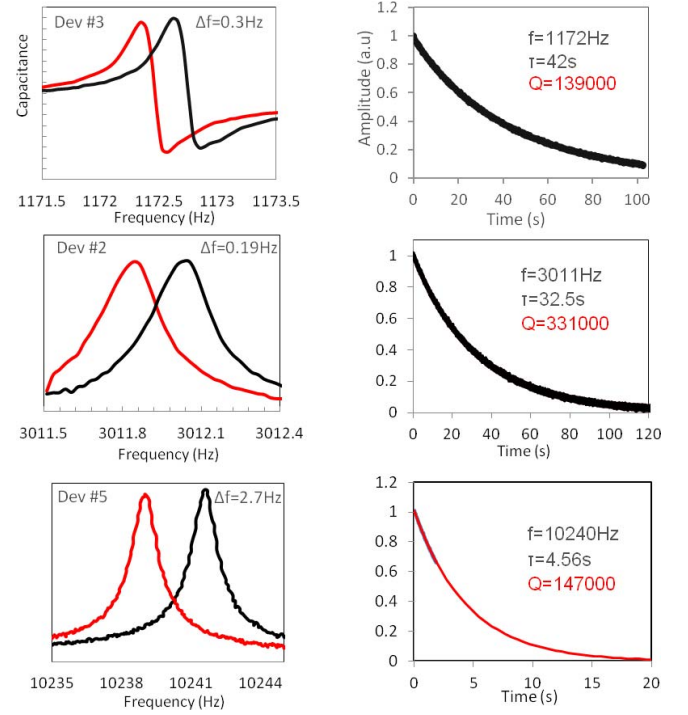


Fig. 11. Experimental results of the as-fabricated frequency response of resonator utilizing concentrated anchor design (left column) at moderate vacuum of around 10Pa. Red color corresponds to the X axis and black color corresponds to the Y axis. Right column shows the decay time and Q-factor under 0.1Pa.

2.3Hz in frequency separation. In table 3, we show the nominal frequency and the frequency separation for other devices, which are grouped by the width of the suspension beams.

The Q -factor of the devices was characterized under 0.1Pa vacuum. We used the ring-down time measurement with the setup shown in Fig. 8. Input frequency, f_r , was manually tuned to produce the largest amplitude after the demodulator. Then, the input signal was cut off, while keeping the carrier frequency, f_r , and DC voltage applied to the proof-mass. The decay time was recorded using the Plotter function in the LabOne software interface which controls the Zurich Instrument Lock-in amplifier. The decay time is the time required for the amplitude, A , to decay below A/e , where $e = 2.7182$. The normalized amplitude decay time was recorded for three devices. Experimental results are shown in the right column of Fig. 10. The Q factor was calculated using

$$Q = f_r \cdot \pi \cdot \tau \quad (4)$$

where f_r is the resonant frequency in Hz and τ is the decay time in seconds.

Note that the frequency sweep and the ring-down time measurements of the Q factor are different due the use of different pressure in the vacuum chamber.

C. Temperature Stability

The device #2 with the operational frequency of 3kHz was vacuum packaged at a moderate vacuum under pressure around 5 Pa (corresponding to the Q factor of 15,000) and

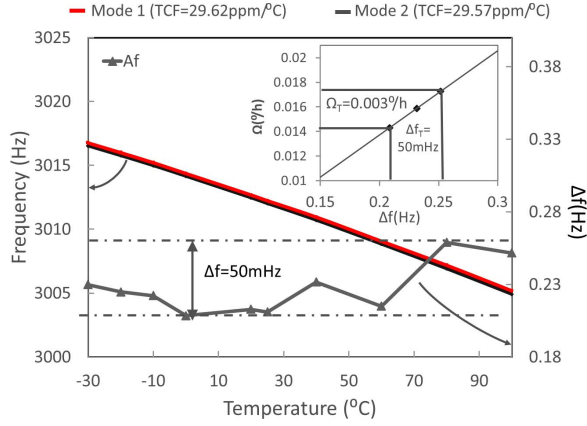


Fig. 12. TCF and Δf characterization. Concentrated anchor design showed 0.12ppm/°C stability of the frequency split. Inset shows the effect of the TCF on the angle estimation (we assumed $\Delta(1/\tau) = 0$ and $Q = 330k$).

placed inside the thermal chamber ESPEC SH-240, with a temperature control in the range from -30°C to 100°C . The thermal chamber was manually controlled and the temperature fluctuation inside the chamber was $\pm 0.5^\circ\text{C}$. After setting the reference temperature, we allowed 30 minutes for the MEMS to thermally stabilize. Figure 12 shows the experimental results. The resonant frequencies of the drive and sense modes were recorded during the incremental temperature sweep. The measured temperature coefficient of the resonant frequency (TCF) was 29.62ppm/°C for the sense mode and 29.57ppm/°C for the drive mode. The frequency symmetry (Δf) variation was under 50mHz for the 130°C range when the resonant frequency of the drive and sense mode was measured. The temperature fluctuation inside the thermal chamber of $\pm 0.5^\circ\text{C}$ introduced a frequency error of 89mHz in each frequency measurement. If we estimate the frequency variation from the temperature coefficient extracted from the measurement of the resonator frequency in the x and y modes, the frequency split variation is estimated to be on the order of 23.5mHz. For RIG mechanization, the corresponding angle drift due to variation of the Δf can be estimated using equation (1). For simplicity we assumed $1/\tau = 0$, and the angle drift due to the thermal effects was estimated to be on the level of $0.003^\circ/\text{hr}$. This suggests that we can relax our requirements on the frequency split control under thermal variation, as in the present study this effect is almost two orders of magnitude lower.

D. Gyroscope Characterization

Rate sensitivity and gyroscope performance were experimentally demonstrated for the vacuum sealed (under 7Pa) Device #2, operating at 3011Hz with a Q -factor of 5000 (Q -factor degraded from 10,000 to 5,000 over six months' time due to the lack of getter material inside the package). The resonator was electrostatically tuned down to 10mHz by using the tuning voltage on the level of 1.6V, which was applied to the drive forcer electrodes. Frequency response for the drive and sense modes are shown in Fig. 13. Lower tuning voltage can be used if the forcer and pick off electrodes are used for tuning.

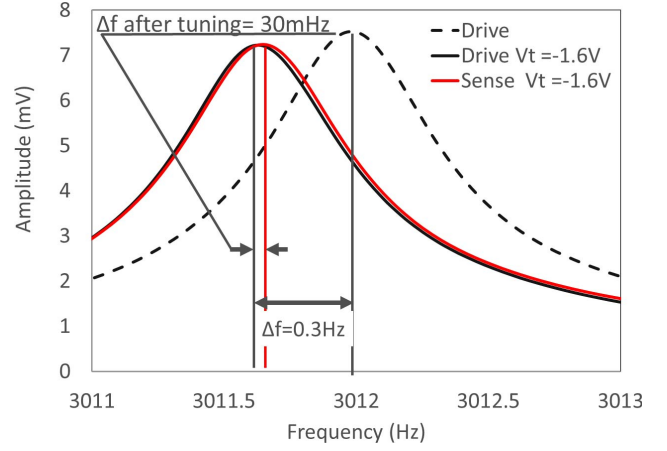


Fig. 13. Frequency response of device #2, before and after electrostatic tuning.

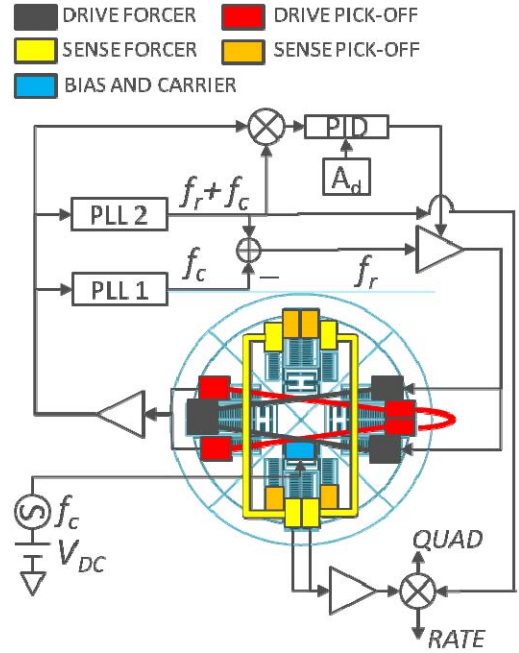


Fig. 14. Open loop gyroscope mechanization scheme.

For the gyroscope operation, the resonator was electrostatically forced to oscillate at the resonance in the out-of-phase mode along the x axis. EAM, as described in section IV.A, was used to decouple the frequency of the parasitic current from the mechanical resonance. The experimental setup is described in Fig 14. A carrier signal with 1V of amplitude, bias voltage of 5V, and frequency f_c of 100kHz were applied to suspended masses using an external signal generator. An excitation signal at the resonant frequency of the device, $f_r = 3,011\text{Hz}$, was generated using the AM modulation capability of the HF2LI, as in [29]. The PLL1 was locked to the carrier frequency, f_c , and PLL2 was locked at the frequency $f_c + f_r$. The PLL 2 frequency was subtracted by the PLL1 frequency to generate the drive frequency f_r . The drive amplitude was demodulated at the frequency of the PLL2 and the in-phase component of the demodulated signal was utilized to maintain the mechanical amplitude of around 1μm.

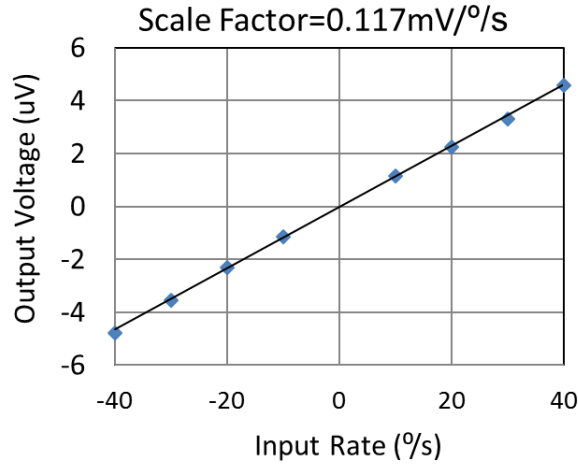


Fig. 15. Scale factor of the concentrated spring resonator operated in the Rate mode.

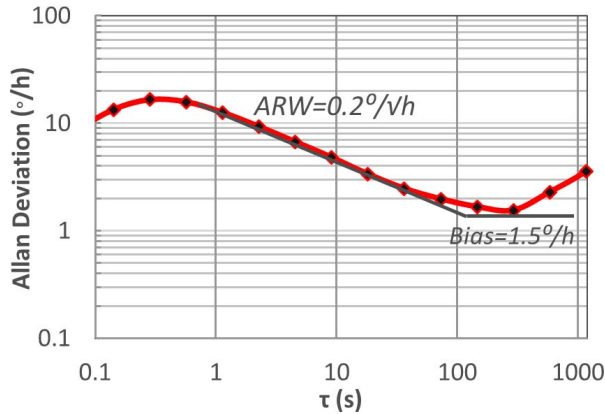


Fig. 16. Allan variance of concentrated spring resonator operated in Rate Gyroscope (RG) mode.

The sense pick-off electrodes were connected to the input of the lock-in amplifier via a trans-impedance amplifier with a 100kΩ feedback resistor and the second stage 10x amplifier. The signal was demodulated using the sideband frequency of 103,011 KHz and separated to in-phase and quadrature – phase components.

The gyroscope was placed on a custom-built rate table. The scale factor was evaluated at the input rate ranging between ± 40 dps (Fig. 15) and measured to be 117uV/ deg/s.

The zero-rate output (ZRO) was measured for 7h with the sampling rate of 224 Hz and without the temperature control. The Quadrature null feedback loop was enabled to maintain the quadrature signal at 0. The Allan variance was derived based on these measurements. The Allan Variance at 1 second, or Angle Random Walk, was measured at 0.2deg/ $\sqrt{\text{Hz}}$. This value is bigger than the theoretical ARW, suggesting that other effects besides the thermo-mechanical noise are dominating performance of the gyro. The minimum of the Allan variance was found after 200 seconds of the integration time, measuring a bias instability of 1.5dph (Fig. 16). Bias instability is expected to decrease by operating the device at higher levels of vacuum and using temperature compensation or feedback thermal control of the unit.

V. CONCLUSIONS

In this work we explored the effects of concentrating of the sensitive elements – mechanical springs and anchors – of the mass-balanced degenerate mode gyroscopes in a small central area of the sensor to achieve a sub-Hz frequency separation between the drive and the sense modes. The use of the concentrated springs allows to maintain a tight frequency symmetry even under thermal stress conditions. We observed less than 50mHz frequency variation in a range of temperatures from -30 to 100 °C. The gyroscope operation at low as-fabricated frequency split allows to lower voltages to tune the resonator and subsequently reduce the noise induced by the voltage supply. Reported results are a step toward achieving a low bias instability Rate Integrating gyroscope that will be required for high precision inertial navigation applications.

REFERENCES

- [1] D. Senkal, A. Efimovskaya, and A. M. Shkel, "Minimal realization of dynamically balanced lumped mass WA gyroscope: Dual focault pendulum," in *Proc. IEEE Int. Symp. Inertial Sensors Syst. (INERTIAL)*, Hapuna Beach, HI, USA, Mar. 2005, pp. 1–2.
- [2] A. A. Trusov *et al.*, "Force rebalance, whole angle, and self-calibration mechanization of silicon MEMS quad mass gyro," in *Proc. IEEE Int. Symp. Inertial Sensors Syst. (INERTIAL)*, Laguna Beach, CA, USA, Feb. 2014, pp. 1–2.
- [3] D. D. Lynch, "MRIG frequency mismatch and quadrature control," in *Proc. Int. Symp. Inertial Sensors Syst. (INERTIAL)*, Laguna Beach, CA, USA, Feb. 2014, pp. 1–4.
- [4] Y.-W. Lin, S. Lee, S.-S. Li, Y. Xie, Z. Ren, and C. T.-C. Nguyen, "Series-resonant VHF micromechanical resonator reference oscillators," *IEEE J. Solid-State Circuits*, vol. 39, no. 12, pp. 2477–2491, Dec. 2004.
- [5] M. A. Abdelmoneum, M. U. Demirci, and C. T.-C. Nguyen, "Stemless wine-glass-mode disk micromechanical resonators," in *Proc. 16th Annu. Int. Conf. Micro Electro Mech. Syst. (IEEE MEMS)*, Kyoto, Japan, Jan. 2003, pp. 698–701.
- [6] S. Askari, M. H. Asadian, K. Kakavand, and A. M. Shkel, "Vacuum sealed and getter activated MEMS quad mass gyroscope demonstrating better than 1.2 million quality factor," in *Proc. IEEE Int. Symp. Inertial Sensors Syst. (INERTIAL)*, Laguna Beach, CA, Feb. 2016, pp. 142–143.
- [7] P. Taheri-Tehrani *et al.*, "Epitaxially-encapsulated quad mass gyroscope with nonlinearity compensation," in *Proc. IEEE 29th Int. Conf. Micro Electro Mech. Syst. (IEEE MEMS)*, Shanghai, China, Jan. 2016, pp. 966–969.
- [8] D. Senkal, A. Efimovskaya, and A. M. Shkel, "Dual focault pendulum gyroscope," in *Proc. 18th IEEE Int. Conf. Solid-State Sens., Actuators Microsyst. (TRANSDUCERS)*, Anchorage, AK, USA, Jun. 2015, pp. 1219–1222.
- [9] A. Efimovskaya, Y.-W. Lin, D. Wang, and A. M. Shkel, "Electrostatic compensation of structural imperfections in dynamically amplified dual-mass gyroscope," in *Proc. IEEE Int. Symp. Inertial Sensors Syst. (INERTIAL)*, Kauai, HI, USA, Mar. 2017, pp. 1–4.
- [10] R. Gando *et al.*, "A MEMS rate integrating gyroscope based on catch-and-release mechanism for low-noise continuous angle measurement," in *Proc. IEEE Micro Electro Mech. Syst. (MEMS)*, Belfast, U.K., Jan. 2018, pp. 944–947.
- [11] H. H. Ge, D. Kim, and R. M'Closkey, "Simultaneous exploitation of the fundamental and higher order wineglass modes in a vibratory gyro," in *Proc. IEEE Int. Symp. Inertial Sensors Syst. (INERTIAL)*, Hapuna Beach, HI, USA, Mar. 2015, pp. 1–4.
- [12] C. H. Ahn *et al.*, "Mode-matching of wineglass mode disk resonator gyroscope in (100) single crystal silicon," *IEEE J. Microelectromech. Syst.*, vol. 24, no. 2, pp. 343–350, Apr. 2015.
- [13] J. Ren *et al.*, "A mode-matching 130-kHz ring-coupled gyroscope with 225 ppm initial driving/sensing mode frequency splitting," in *Proc. 18th Int. Conf. Solid-State Sens., Actuators Microsyst. (TRANSDUCERS)*, Anchorage, AK, USA, Jun. 2015, pp. 1057–1060.
- [14] M.-L. Chan *et al.*, "Micromachined polycrystalline diamond hemispherical shell resonators," in *Proc. Solid-State Sens., Actuators Microsyst. Workshop (Hilton Head)*, Hilton Head Island, SC, USA, Jun. 2012, pp. 2415–2418.

- [15] Y. Xie, H.-C. Hsieh, P. Pai, H. Kim, M. Tabib-Azar, and C. H. Mastrangelo, "Precision curved micro hemispherical resonator shells fabricated by poached-egg micro-molding," in *Proc. IEEE Sensors Conf. (SENSORS)*, Taipei, Taiwan, Oct. 2012, pp. 1–4.
- [16] J. Cho, J. Yan, J. A. Gregory, H. Eberhart, R. L. Peterson, and K. Najafi, "High- Q fused silica birdbath and hemispherical 3-D resonators made by blow torch molding," in *Proc. IEEE 26th Int. Conf. Micro Electro Mech. Syst. (IEEE MEMS)*, Taipei, Taiwan, Jun. 2013, pp. 177–180.
- [17] D. Senkal, M. J. Ahamed, A. A. Trusov, and A. M. Shkel, "Achieving sub-Hz frequency symmetry in micro-glassblown wineglass resonators," *IEEE J. Microelectromech. Syst.*, vol. 23, no. 1, pp. 30–38, Feb. 2014.
- [18] D. M. Rozelle, "The hemispherical resonator gyro: From wineglass to the planets," in *Proc. AAS/AIAA Space Flight Mech. Meeting*, 2009, pp. 1157–1178.
- [19] Z. Hou, X. Wu, D. Xiao, X. Wang, and Z. Chen, "Modal coupling error suppression in micromachined gyroscopes by UV laser trimming," in *Proc. IEEE Sensors Conf. (SENSORS)*, Busan, South Korea, Nov. 2015, pp. 1–4.
- [20] D. Kim and R. M'Closkey, "A MEM vibratory gyro with mode-matching achieved by resonator mass loading," in *Proc. IEEE/ION Position, Location Navigat. Symp. (PLANS)*, Monterey, CA, USA, May 2014, pp. 499–503.
- [21] S. Sonmezoglu, S. E. Alper, and T. Akin, "A high performance automatic mode-matched MEMS gyroscope with an improved thermal stability of the scale factor," in *Proc. 17th Int. Conf. Solid-State Sens., Actuators Microsyst. (TRANSDUCERS EUROSENSORS XXVII)*, Barcelona, Spain, Jun. 2013, pp. 2519–2522.
- [22] Z. X. Hu, B. J. Gallacher, J. S. Burdess, C. P. Fell, and K. Townsend, "Precision mode matching of MEMS gyroscope by feedback control," in *Proc. IEEE Sensors Conf. (SENSORS)*, Limerick, Ireland, Oct. 2011, pp. 16–19.
- [23] D. M. Tanner, A. C. Owen, and F. Rodriguez, "Resonant frequency method for monitoring MEMS fabrication," *Proc. SPIE*, vol. 4980, pp. 220–228, Jan. 2003.
- [24] J. Giner, Y. Zhang, D. Maeda, K. Ono, A. M. Shkel, and T. Sekiguchi, "Dynamically balanced degenerate mode gyro with sub-Hz frequency symmetry and temperature robustness," in *Proc. 30th Int. Conf. Micro Electro Mech. Syst. (IEEE MEMS)*, Las Vegas, NV, USA, Jan. 2017, pp. 1103–1106.
- [25] R. P. Leland, "Mechanical-thermal noise in MEMS gyroscopes," *IEEE Sensors J.*, vol. 5, no. 3, pp. 493–500, Jun. 2005.
- [26] D. Maeda, H. Jeong, K. Yamanaka, and M. Hayashi, "Deformation-robust gyroscope with 2.0-Hz frequency split variation over temperature range of -50 to 150 °C," in *Proc. Int. Symp. Inertial Sensors Syst. (INERTIAL)*, Laguna Beach, CA, USA, Mar. 2014, pp. 1–4.
- [27] *MEMS+ Overview*. Accessed: May 23, 2017. [Online]. Available: <http://www.coventor.com/mems-solutions/products/mems-plus-overview/>
- [28] *CoventorWare*. Accessed: May 11, 2017. [Online]. Available: <http://www.coventor.com/mems-solutions/products/coventorware>
- [29] *Control of MEMS Coriolis Vibratory Gyroscopes*. [Online]. Available: https://www.zhinst.com/sites/default/files/zi_appnote_mems_gyroscope.pdf



Joan Giner (M'12) received the bachelor's degree in telecommunication engineering, the M.S. degree in micro and nanotechnologies, and the Ph.D. degree in electronic engineering from the Universitat Autònoma de Barcelona, Spain, in 2007, 2008, and 2012, respectively.

In 2012, he joined the University of California, Irvine, CA, USA, for a two-year postdoctoral stage with the Micro Systems Laboratory, after receiving the Balsells Fellowship in the frame of a collaborative program between the Catalan Government, Spain, and the State of California, USA. At UCI, he was involved in the fabrication and characterization of spherical microresonators. In 2015, he joined Hitachi Central Research Laboratory, Japan, as Visiting Researcher. Since 2018, he works at GlobalFoundries Pte., Singapore. His interests center on the design and fabrication of micro-machined structures for inertial, biometric, and RF applications. He currently serves as Review Committee Member for the IEEE International Symposium on Inertial Sensors and Systems.



in the area of sensing applications and data science.

Daisuke Maeda received the B.E. and M.E. degrees in computer science from the Toyohashi University of Technology, Aichi, Japan, in 2005 and 2007, respectively. In 2007, he joined Hitachi Ltd., Tokyo, Japan, where he has been involved in the development of micro-electromechanical inertial sensors and sensor systems. He also worked for Hitachi Automotive Systems Inc., Ibaraki, Japan, from 2016 to 2018, as a Production Engineer. He is currently working with Hitachi America Ltd., Santa Clara, CA, USA, as a Research Engineer, where he has been involved



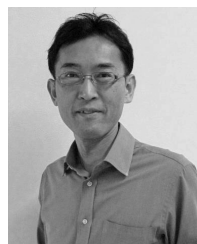
Kazuo Ono was born in Fujinomiya, Japan, in 1978. He received the B.E., M.E., and D.E. degrees from the University of Tokyo, Tokyo, Japan, in 2001, 2003, and 2006, respectively.

In 2006, he joined the Central Research Laboratory, Hitachi, Ltd., Tokyo, where he has been involved in the Research and Development of emerging memory technology. In 2009, he developed spin-transfer torque memory and its applications. He was a Visiting Industrial Fellow at the Mechanical Engineering Department, University of California, Berkeley, CA, USA, under the supervision of Prof. A. Pisano, from 2012 to 2013. He was involved in the development of microelectromechanical system inertial sensors for automotive application from 2013 to 2017. He moved to the Hitachi Insight Group Control System Platform Division, Omika Works, in 2018. His current interests are on IoT sensing technology with low power wireless communication and sensors. He received the Young Researcher Award from SSDM 2009.



Andrei M. Shkel (F'99) received the Diploma degree (Hons.) in mechanics and mathematics from Moscow State University, Moscow, Russia, in 1991, and the Ph.D. degree in mechanical engineering from the University of Wisconsin, Madison, WI, USA, in 1997.

In 2000, he joined the Faculty at the University of California at Irvine, Irvine, CA, USA, where he is currently a Professor with the Department of Mechanical and Aerospace Engineering, with a joint appointment in the Department of Electrical Engineering and Computer Science, and the Department of Biomedical Engineering. He served as the Program Manager of the Microsystems Technology Office, Defense Advanced Research Projects Agency, Arlington, VA, USA, from 2009 to 2013. His professional interests are reflected in over 200 publications. He holds over 40 U.S. patents. His current interests center on the design, manufacturing, and advanced control of precision micromachined gyroscopes. He was a recipient of the 2002 George E. Brown, Jr. Award, the 2005 NSF CAREER Award, the 2006 UCI HSSoE Best Faculty Research Award, and the 2009 IEEE Sensors Council Technical Achievement Award. In 2013, he received the Office of the Secretary of Defense Medal for Exceptional Public Service. He has served on a number of editorial boards, most recently, as an Editor of the IEEE/ASME JOURNAL OF MICROELECTROMECHANICAL SYSTEMS, the Associate Editor-in-Chief of the IEEE SENSORS LETTERS, the Editorial Board Member of the *Journal of Gyroscopy and Navigation*, and the Founding Chair of the IEEE International Symposium on Inertial Sensors and Systems. He was voted as the 2018 President-Elect of the IEEE Sensors Council.



Tomonori Sekiguchi (M'93) received the B.S., M.S., and Ph.D. degrees from the Tokyo Institute of Technology, Tokyo, Japan, in 1991, 1993, and 2012, respectively. He joined the Central Research Laboratory, Hitachi, Ltd., Tokyo, in 1993. He was involved in the research of DRAMs from 1993 to 2010.

He was a Visiting Researcher with the Integrated Systems Laboratory, Swiss Federal Institute of Technology Zürich, from 2002 to 2003. He contributed to the R&D planning in the European Research and Development Centre, Hitachi Europe Ltd., U.K., from 2010 to 2014. He is currently with the R&D Group, Hitachi Ltd., Tokyo, where he has been involved in the research of MEMS sensors and application systems. He served as a member of the program committee of the Symposium on VLSI Circuits from 2006 to 2010.